Insertion layer magnetism detection and analysis using transverse magneto-optical Kerr effect (T-MOKE) ellipsometry

Carmen Martín Valderrama[1], Mikel Quintana[1], Ane Martínez-de-Guerenu[2,3], Tomoki Yamauchi[4], Yuki Hamada[4], Yuichiro Kurokawa[4], Hiromi Yuasa[4], and Andreas Berger[1]

[1] CIC nanoGUNE BRTA, Tolosa Hiribidea 76, E-20018 Donostia – San Sebastían, Spain
[2] CEIT-Basque Research and Technology Alliance (BRTA), Manuel Lardizabal 15, E-20018 Donostia – San Sebastían, Spain
[3] Universidad de Navarra, Tecnun, Manuel Lardizabal 13, E-20018 Donostia – San Sebastían, Spain
[4] Faculty of Information Science and Electrical Engineering, Kyushu University, Fukuoka 819-0395, Japan

Abstract

This experimental study demonstrates that with transverse magneto-optical Kerr effect (T-MOKE) ellipsometry, it is possible to determine the magneto-optical and magnetic properties of insertion layers, even if they are superimposed onto much bigger magnetic signals from the surrounding structure. Hereby, it turns out to be especially valuable that with T-MOKE ellipsometry one has full and precise quantitative access to the complex value of the magneto-optical reflection matrix component $\tilde{\beta}$, because small magneto-optical insertion layer signals do not necessarily increase the absolute size of $\tilde{\beta}$, but can lead to observable phase changes of this complex quantity instead. We demonstrate the ability of T-MOKE ellipsometry to detect such small effects precisely and hereby allow for an accurate determination of the alloy concentration dependent onset of ferromagnetism in ultrathin Co_xRu_{1-x} insertion layers, that are embedded into a much thicker ferromagnetic structure. In addition, a detailed and quantitative signal analysis allowed us to demonstrate that the Co_xRu_{1-x} insertion layers in our samples exhibit a magnetization reversal behavior that is independent from the adjacent $Y_3Fe_5O_{12}$ (YIG) layers, clearly indicating that both magnetic entities are either not or only very weakly coupled.

1. Introduction

Magnetic multilayers fabricated as stacked sequences of different ferromagnetic and non-magnetic layers on the nm-scale have long been a most relevant research topic and a key ingredient in technologies, in particular information storage technologies [1]. The reason for this tremendous relevance of ferromagnetic multilayers stems from the fact that due to the quantum mechanical nature of the electronic states at and near interfaces, magnetic and associated properties can be changed in a very relevant way and achieve behavior that would otherwise not be accessible [2]. The most prominent example of this is interlayer exchange coupling, in which the collective magnetic behavior depends on the thickness and electronic properties of a non-magnetic insertion layer that is placed in between ferromagnetic films, so that it can mediate an effective ferromagnetic, antiferromagnetic or even helical coupling in between them [3-6]. Another example is the interface induced anisotropy, which can be strongly enhanced by alternating ferromagnetic films with non-magnetic materials that exhibit strong spin-orbit coupling, and can lead to strong perpendicular magnetic anisotropy, as for instance in Co/Pt multilayers [7-9]. The specific properties and spin-states of such non-ferromagnetic insertion layers furthermore impact electronic transport properties, of which the giant magneto-resistance (GMR) is the most famous and most impactful example [10,11]. More recently, other transport properties were also shown to be very relevantly impacted by magnetic multilayer structures [12] or the use of special insertion layers at the interface [13]. For instance, it was reported that the spin-Seebeck effect is modified by the magnetic materials properties of insertion layers [14,15].

Associated with an unambiguous interpretation of any of these phenomena is the need to identify the spin or magnetization state of these insertion layers, given that their magnetic and magneto-electric properties are associated with the resulting spin state that is present upon multilayer stacking of such structures [16]. Commonly, the resulting spin state is caused by the hybridization and intermixing of the electronic states at interfaces, given the delocalized nature of the electron wave functions, which can lead to rather long-ranging perturbations, such as spin polarized quantum well states in metallic multilayers, for example [17,18]. In general, the experimental identification of such insertion layer magnetic states is a formidable task, given that their typically weak magnetic signature is superimposed onto a very strong magnetic signal coming from the

magnetic materials in such multilayers, rendering conventional magnetometry useless. Also, insertion layers are, by definition, sub-surface layers, so that extremely surface sensitive methods are mostly not suitable either.

There are, of course, numerous good examples of analyzing the magnetic state of insertion layers in magnetic multilayers and do so very precisely. The most successful technique and thus the most-commonly used methodology is X-ray magnetic circular dichroism, which is in principle capable of identifying subsurface magnetic insertion layer magnetism [19-21]. However, despite its successes, it is methodologically complex, needs large scale facilities and only works if the insertion layer's elemental composition does not overlap with elements used in the rest of the structure, which can be a very limiting condition. On the other hand, it is well known that magneto-optics is very sensitive to detect magnetism even in single atomic layers and can do so by utilizing widely applicable and cost-effective experimental setups [22-26]. Furthermore, there have been a number of studies that were able to identify an interface- or depth-dependent contribution to magneto-optical signals [27-30]. Thus, it is conceivable that a magneto-optical measurement approach also allows the separate detection of insertion layer magnetism, even if this insertion layer signal is superimposed onto a much larger signal coming from other layers that are part of multilayer structures. There have been successful attempts in the past to separate magneto-optical signals coming from different individual layers in multilayer sequences, either by tuning the angle-of-incidence or optical wavelengths [31-33], but these studies were analyzing signal superpositions of magnetic layers that produced similar sized signals. Thus, the detection of specific signals coming from an insertion layer, being a minor contributor to the overall magnetism of a multilayer structure is an outstanding problem and experimental challenge. The very goal and purpose of this study is to address this challenge, which we pursue here by means of the recently developed transverse magneto-optical Kerr effect (T-MOKE) ellipsometry [34].

2. Experimental Approach

The specific type of sample that we study here is schematically shown in Fig. 1(b). Our samples consist primarily of a 50 nm thick $Y_3Fe_5O_{12}$ (YIG) film, which is the main magnetic layer and which has been grown directly onto naturally oxidized Si-wafers by means of

sputter deposition and subsequent annealing in atmosphere at 750ºC for 1 hour. This produced polycrystalline films with large lateral grains and a texture that induces an in-plane alignment of the YIG magnetization, which we have verified by means of conventional magnetometry, and associated magnetoelectric transport measurements [15]. On the top of each sample is a 1 nm thick Pt layer that has been sputter deposited as well. In between these two layers, there is a CoRu alloy insertion layer that is the focus of this investigation. All Co_xRu_{1-x} films are grown by co-sputter deposition, they are precisely 2 nm thick and each of them has a predefined composition in the range from $x = 0.75$ to $x = 1.00$. The specific thickness and alloy compositions of the insertion layers have been chosen based upon prior and preliminary studies. In a preparatory study, we determined that Co films grown directly onto our 50 nm thick YIG films and covered by 1 nm thick Pt layers exhibit ferromagnetism at room temperature, if the Co film thickness is larger than 1.7 nm. Thus, a 2 nm thick Co film shows robust ferromagnetism, so that alloying it with Ru in the concentration range of $0 - 25\%$ should allow us to tune the Curie temperature of these 2 nm thick CoRu films within the vicinity of room temperature [35], which is the temperature range of interest for our study. So, by varying the CoRu alloy concentration, we should be able to facilitate a most significant change in the magnetic properties of these insertion layers at room temperature, which should furthermore impact the transport properties most relevantly [15]. For any magnetism-based interpretation, it is however crucially important that one can actually detect the magnetism of such insertion layers reliably, keeping in mind that their magnetism is superimposed onto a much larger magnetic response from the much thicker YIG base layer. Hereby, we would like to emphasize that the overall sample structure used here, including the selection of YIG as its base layer material as well as the YIG layer thickness, were not chosen for magneto-optical measurement convenience, but for their utility in magneto-electric and Spin-Seebeck measurements, which is the ultimate goal of this specific layer sequence. Thus, the insertion layer structures, shown here in Fig. 1(b) represent a true utility test case to demonstrate the capabilities of T-MOKE ellipsometry to detect and distinguish insertion layer magnetism. Furthermore, our methodology is not limited to transparent magnetic base layers but is also applicable to multilayers of all metallic films, even if one will have to contend in this case with far stronger attenuation, so that investigations of insertion layers below thick

metallic overcoats will be challenging or even impossible. However, it is worth noticing that our methodology has already demonstrated that it can detect magneto-optical signals even below a 80 nm thick Ag overcoat film [34].

The experimental setup for our ellipsometric T-MOKE methodology is schematically represented in Fig. 1(a) and was discussed in detail in [34]. As a light source, we use a solid-state laser producing light of wavelength λ = 635 nm and we utilize a reflection geometry angle-of-incidence of 60º with respect to the surface normal. The laser light passes through the first linear polarizer P_1, whose polarization axis is oriented at 45º from the plane-of-incidence in this study to generate a balanced mixture of s- and p-polarized light for optimized tool performance [36]. The linear polarized light is then reflected by the sample, which is placed inside the gap of an electromagnet, which produces a magnetic field along the transverse orientation, i.e. perpendicular to the plane-of-incidence. The reflected beam passes through a quarter wave plate QWP and a second linear polarized P_2, whose orientations can be precisely altered by motorized rotation stages. Finally, the transmitted light intensity I is measured with a Si-photodiode detector after passing an optical notch filter to suppress environmental light influences.

For the selected incoming linear polarization, the phase shift between the reflected s- and p-polarized light leads to an elliptical polarization state after sample reflection, which is a pure optical effect and unrelated to magneto-optics in and by itself. Upon appropriately aligning the orientation of QWP and P_2, extinction of this reflected light can be achieved at a particular setting of the element angles θ_2 and Φ_2. In the vicinity of this extinction point, which is characterized by element orientations θ_2^{ext} and Φ_2^{ext}, the set-up is now extremely sensitive to detecting small magneto-optical signals that are caused by the change of p-polarization reflectivity associated with T-MOKE [37-39]. Furthermore, the interplay in between the above mentioned optical ellipticity and magneto-optical induced effects enables a complete determination of the reflection matrix, including the optical Fresnel coefficients, if one combines a series of measurements for different (θ_2,Φ_2) settings [34]. In our measurements here, we utilize a grid of 21 $\times$ 21 (θ_2,Φ_2) settings in an angular range of $\pm$ 4º surrounding the extinction point (θ_2^{ext},Φ_2^{ext}), which then allows for a very precise measurement of the reflection

matrix of the sample, as well as a rigorous self-consistency check of our measurement and data analysis approach. For our set-up, the total intensity at the detector is given by

$$I = \vec{E}_D^* \cdot \vec{E}_D + I_{NM} \qquad (1),$$

where $\vec{E}_D$ is the electric field vector, which arrives at the photodetector due to the reflection of the incoming light, and I_{NM} being a light intensity contribution that is not related to the sample reflection process. Using the Jones calculus, we can compute $\vec{E}_D$ as

$$\vec{E}_D = \underline{P2} \cdot \underline{QWP} \cdot \underline{R} \cdot \vec{E} \qquad (2)$$

with $\underline{P2}$ and $\underline{QWP}$ being the Jones matrices associated with P$_2$ and QWP in the reflected light path, respectively, $\underline{R}$ being the reflection matrix of the sample and $\vec{E}$ being the electric field vector of the incoming light once it has passed through P$_1$. Hereby,

$$\underline{R} = \begin{pmatrix} r_s & 0 \\ 0 & r_p + \beta \end{pmatrix} = r_p \begin{pmatrix} \tilde{r}_s & 0 \\ 0 & 1 + \tilde{\beta} \end{pmatrix} = r_p \underline{\tilde{R}} \qquad (3)$$

is the reflection matrix of the sample that we intend to determine with r_s and r_p being the conventional Fresnel coefficients for s- and p-polarized light and β being the p-polarization reflection contribution that is dependent on T-MOKE [22]. $\tilde{r}_s$ and $\tilde{\beta}$ are equal to r_s and β, respectively, divided by r_p. The detection method of our ellipsometric T-MOKE measurements now utilizes the fact that β changes its value if the transverse magnetization changes, and in particular that it inverts to -β if the transverse magnetization inverts. If we apply this fact in Eq. (3) and further utilize Eqs. (1) and (2), we can demonstrate that the intensity change ΔI at the detector of our setup due to the inversion of the transverse magnetization, normalized by the average intensity I, is given as [34]:

$$\frac{\Delta I}{I} = 4 \frac{B_1 \cdot h_2 + (B_1 B_3 + B_2 B_4) \cdot h_3 - (B_1 B_4 - B_2 B_3) \cdot h_4 + B_6}{\left(B_3{}^2 + B_4{}^2\right) \cdot h_1 + h_2 + 2 \cdot B_3 \cdot h_3 - 2 \cdot B_4 \cdot h_4 + B_5} \tag{4}$$

with

$$h_1 = \frac{cos^2(2\phi_2 - \theta_2)}{2} + \frac{cos^2(\theta_2)}{2} \tag{5a},$$

$$h_2 = \frac{sin^2(2\phi_2 - \theta_2)}{2} + \frac{sin^2(\theta_2)}{2} \tag{5b},$$

$$h_3 = \frac{sin(4\phi_2 - 2\theta_2)}{4} + \frac{sin(\theta_2)}{4} \tag{5c},$$

$$h_4 = \frac{sin(2\phi_2 - 2\theta_2)}{2} \tag{5d},$$

and B_i being the elements of the reflection matrix, specifically:

$$B_1 = Re(\tilde{\beta}) \tag{6a},$$

$$B_2 = Im(\tilde{\beta}) \tag{6b},$$

$$B_3 = Re(\tilde{r_s}) \tag{6c},$$

$$B_4 = Im(\tilde{r_s}) \tag{6d}.$$

Furthermore, B_5 represents the DC value of I_{NM} that is primarily associated with slight imperfections of the optical elements, while B_6 describes the field modulation frequency ω component of I_{NM} that enters the detection circuit either optically or electrically. We find both B_5 and B_6 to be extremely small in our measurements here, and we only mention them for completeness and for consistency with prior work [34]. Given that we now have a complete quantitative description of our optical experiment for any (θ_2, Φ_2) setting, we can use Eq. (4) to fit a sequence of experimental data by

utilizing $B_1 - B_4$ as fit parameters to determine the full reflection matrix of the sample under investigation, which is the strategy of our ellipsometric T-MOKE method [34].

3. Experimental Results

Figure 2 displays our experimental T-MOKE ellipsometry results for the entire set of samples that we have investigated. In all these measurements, we applied a sinusoidal magnetic field sequence of frequency ω = 314 s^{-1} and amplitude H_0 = 370 Oe, after verifying that this field value is sufficient to saturate each sample's magnetization along the transverse direction and accordingly, saturate the associated magneto-optical signal. Every sub-figure in the upper row of Fig. 2, i.e. Figs. 2(a) – (g), shows hereby the measured relative intensity change $\Delta I/I$ as a function of the specific $(\tilde{\theta}_2, \tilde{\Phi}_2)$ setting of our optical elements for an individual sample as a color-coded map. Purely for convenience, we utilize for the graphical representation $\tilde{\theta}_2 = \theta_2 - \theta_2^{ext}$ and $\tilde{\Phi}_2 = \Phi_2 - \Phi_2^{ext}$, which represent the values of θ_2 and Φ_2 as their distance from the extinction point $(\theta_2^{ext}, \Phi_2^{ext})$. Each specific sample is identified by means of the composition parameter x of the insertion layer, shown above the data, while the identifier YIG is referring to a structure without insertion layer. The bottom row of Fig. 2, i.e. Figs. 2(h) – (n), shows the corresponding least-squares fits according to Eq. (4) in direct comparison to the data with the respective coefficient of determination R^2 values of the fits being shown as insets in each figure. The color code that applies to all sub-figures is shown on the right-hand side of Fig. 2. Each experimentally determined $\Delta I/I(\tilde{\theta}_2, \tilde{\Phi}_2)$ data set shows the characteristic ellipsometric T-MOKE signal, with an inversion of the sign of the measured quantity upon crossing the extinction point, and two clearly visible signal peaks on opposite sides of the extinction point, one showing a positive peak and one showing a negative peak [34]. For larger distances from the extinction point $\Delta I/I$ decreases and approaches zero for angular settings outside the here displayed measurement range. Upon comparing experimental data with their respective fits, one can see that both are nearly identical and actually very difficult to distinguish visually. The nearly perfect match of the experimental data to the formal description in Eq. (4) is also reflected in the R^2 values that we determined, which are all larger than 0.996, meaning that the noise level of our data is very low and systematic

deviations in between data and Eq. (4) are basically non-existent [34,36]. This precision demonstrates the relevance of T-MOKE ellipsometry as a precise metrology tool.

If one now compares the results for the different samples in Fig. 2, representing different insertion layers, one observes that except for the pure Co insertion layer, i.e. the x = 1.00 case, all signal pattern look very similar to each other and furthermore very similar to the results of the sample without insertion layer, labelled as YIG. This observation applies to both, the shape of the $\Delta I/I(\tilde{\theta}_2,\tilde{\Phi}_2)$ signal pattern as well as its amplitude, and thus seems to indicate that only the pure Co insertion layer, i.e. x = 1.00, actually produces a significant magneto-optical signal and therefore exhibits magnetism. This interpretation seems to be corroborated, if one considers only the total size of the T-MOKE effect, i.e. abs($\tilde{\beta}$) shown in Fig. 3(a) as a function of the insertion layer Co concentration x, displayed in Figs. 2(h) – (n). As we can see, abs($\tilde{\beta}$) appears to stay nearly constant for x < 1.00 and enhances relevantly only for x = 1.00, i.e. the pure Co insertion layer. Furthermore, all values for abs($\tilde{\beta}$) for x < 1.00 are below the value for the YIG reference sample without insertion layer, shown as a dashed line in Fig. 3(a), which is the expected behavior for non-magnetic insertion layers, given that the magneto-optical signal coming from the YIG layer is somewhat attenuated by such 2 nm thick metallic insertion layers.

However, this initial analysis overlooks the fact that $\tilde{\beta}$ is a complex quantity, just like all other contributions to the Fresnel coefficients in Eq. (3). So, given that $\tilde{\beta}$ is the sum of two possible contributions in our samples, one from the YIG film $\tilde{\beta}_{YIG}$ and one from the CoRu insertion layer $\tilde{\beta}_{CoRu}$, and allowing for the possibility that these contributions have a phase shift of more than 90º, it might happen that the initial occurrence of non-vanishing values for $\tilde{\beta}_{CoRu}$ and thus magnetism in the CoRu insertion layer actually leads to a reduction of abs($\tilde{\beta}$). Such a scenario should be easily visible if one monitors the phase of $\tilde{\beta}$ defined as

$$\phi_{\tilde{\beta}} = arctan\left(\frac{B_2}{B_1}\right) + 180º \qquad (7)[1],$$

---

[1] Given the fact that the real part of $\tilde{\beta}$ is negative for all samples in our measurements, an angle of 180º needs to be added to the conventionally defined arctan-function, given that its values are restricted to -90º to +90º.

which we have done for our measurements as shown in Fig. 3(b). Here, we can see that for $x > 0.80$, there is a continuous change in $\phi_{\tilde{\beta}}$ with x, which implies that for $x > 0.80$, the CoRu insertion layers in our samples are magnetic. We also see that the total change in $\phi_{\tilde{\beta}}$ is larger than 90º, if one changes the Co concentration of the insertion layer from $x = 0.75$ to $x = 1.00$, which is consistent with the above interpretation, that abs($\tilde{\beta}$) might not simply increase and thus does not allow for an easy detection of modest levels of magnetism in the insertion layer. Instead, the large phase shift in between $\tilde{\beta}_{YIG}$ and $\tilde{\beta}_{CoRu}$ should lead to an initial reduction of abs($\tilde{\beta}$) once magnetism in the CoRu insertion layer first occurs, and produce an abs($\tilde{\beta}$) minimum at an intermediate x-value. This behavior is actually visible in Fig. 3(a) upon closer inspection, even if the abs($\tilde{\beta}$) reduction in our samples is rather modest. The minimum of abs($\tilde{\beta}$) occurs for $x = 0.90$. Thus, our T-MOKE ellipsometry measurements evidently contain very relevant information about the magnetic state of the insertion layer, even if they only lead to seemingly minor changes in the experimental signal pattern.

To analyze our experimental data in a more quantitative manner, we now formalize the assumption that the total observed T-MOKE signal $\tilde{\beta}$ in all our samples can be represented as

$$\tilde{\beta} = \tilde{\beta}_{YIG} + \tilde{\beta}_{CoRu} \tag{8}.$$

While it is basically always justified to equate the total MOKE signal of a multilayer structure as the sum of individual layer contributions due to the small perturbation nature of magneto-optics [22,40], we make an additional assumption in formulating Eq. (8), namely that the YIG contribution is always the same, independent of x. This is not a trivial statement, because the quantity $\tilde{\beta}_{YIG}$ includes the attenuation of the YIG generated magneto-optical signal that occurs in the CoRu and Pt layers on top of it and thus, it is formally dependent on x. However, in our measurements, we find B_3 and B_4, i.e. the conventional optical Fresnel coefficients to be independent of x due to the optical similarity of all our CoRu alloys. Thus, their optical constants must be virtually

independent from their alloy concentration at our chosen wavelength, so that the here made assumption of $\tilde{\beta}_{YIG}$ being the same for all x is well justified.

Furthermore, we now assume that the T-MOKE signal of the CoRu alloys is proportional to their magnetization M and that the proportionality constant $\tilde{\beta}_{ins}$ is the same for each insertion layer, and thus independent from x, resulting in

$$\tilde{\beta}(x) = \tilde{\beta}_{YIG} + \tilde{\beta}_{ins} \cdot M(x) \tag{9}$$

The assumption that all CoRu alloy compositions x can be represented by a single pre-factor is an obvious simplification, but a very reasonable one, given that in CoRu alloys both the magnetic moment and the spin-orbit coupling is dominated by the electronic states of the Co atoms. We recently confirmed this fact in studies on epitaxial CoRu films in the here utilized concentration range by showing that both magnetization and magneto-crystalline anisotropy exhibit the same alloy concentration x dependence [35,41]. Equation (9) now implies that the experimental data of all our samples can be traced back to two fixed $\tilde{\beta}$-values, $\tilde{\beta}_{YIG}$ and $\tilde{\beta}_{ins}$, and an insertion layer concentration x dependent magnetization M. The solid green lines in Figs. 3(a) and (b) are the representation of Eq. (9) in comparison to our data, and Fig. 3(c) shows the corresponding magnetization values as a function of x. As we can observe in Figs. 3(a) and (b), our experimental values for abs($\tilde{\beta}$) and $\phi_{\tilde{\beta}}$ are extremely well reproduced by Eq. (9), which is a further confirmation of the assumptions that we made in deriving it. The resulting magnetization values, normalized to the magnetization value of Co, now demonstrate that it is not only the pure Co insertion layer with $x = 1.00$ that exhibits magnetism, but that a detectable magnetization is present in the insertion layers for $x > 0.80$ and that there is a substantial and monotonous increase of M with x. Thus, these measurements demonstrate that we accomplished the tuning of insertion layer magnetization by varying its alloy composition and that we succeeded in separately characterizing the magnetization in our insertion layers by means of T-MOKE ellipsometry.

Our T-MOKE ellipsometry measurements also enable us to study the magnetization reversal behavior in both layers and investigate if they reverse

synchronously or not. Given that the M vs. H hysteresis loop response of a ferromagnetic system generally exhibits strong non-linearities and given that $\tilde{\beta}$ is proportional to the transverse magnetization M along the field direction, the time-dependent intensity $I(t)$ that we measure in our setup is not a purely sinusoidal function but has higher harmonic contributions, even if the applied field H(t) is exactly sinusoidal [34,36]. Figure 4 shows the leading contributions to the $\Delta I/I(\tilde{\theta}_2, \widetilde{\Phi}_2)$ signal pattern at frequencies ω, 3ω, 5ω, and 7ω for two specific samples, namely the YIG sample without insertion layer (left column) and the $x = 0.95$ sample (right column). As one can see from the color-code identification bars on the right-hand side, the higher harmonic signals are substantially smaller than the fundamental signal at ω but given the excellent signal-to-noise performance of our setup, they are easily detectable with high precision [34,36].

Analogous to the data analysis of the saturated signal pattern $\Delta I/I(\tilde{\theta}_2, \widetilde{\Phi}_2)$, we can now fit Eq. (4) to each frequency component separately and from the respective fit parameters determine the frequency specific contribution to the magneto-optical effect, such as $\tilde{\beta}_\omega$ for instance for the ω signal pattern. Given that the general frequency ν dependence of our magneto-optical signals is caused exclusively by the specific time dependence of the magnetization reversal under the utilized field excitation, we find

$$\tilde{\beta}_\nu = \tilde{\beta} \cdot m_\nu \tag{10}$$

with $\tilde{\beta}$ being the sample specific magneto-optical response for saturated magnetization states and m_ν being the normalized magnetization reversal contribution at frequency ν. Given that m_ν is a quantity defined by real values, the resulting signal pattern shape should be identical and produce the same complex phase angle value $\phi_{\tilde{\beta}_\nu}$ for all frequencies ν if the measurements are associated with a single magnetic system. This is exactly what we observe for the YIG sample without insertion layer, shown in Figs. 4(a) – (d), which all exhibit the same pattern and identical $\phi_{\tilde{\beta}_\nu}$ values for ω, 3ω, 5ω, and 7ω.

However, we observe that for the $x = 0.95$ sample, shown in Figs. 4 (e) – (h), the signal patterns are different for different frequencies. From the analysis in Fig. 3, we know that this insertion layer is magnetic and that correspondingly the magneto-optical

signal has two contributions, namely $\tilde{\beta}_{YIG}$ and $\tilde{\beta}_{CoRu}$. Thus, the frequency separated magneto-optical response of this sample also has two contributions and is given as

$$\tilde{\beta}_\nu = \tilde{\beta}_{YIG} \cdot m_\nu^{YIG} + \tilde{\beta}_{CoRu} \cdot m_\nu^{CoRu} = \left(\tilde{\beta}_{YIG} + \tilde{\beta}_{CoRu} \cdot \frac{m_\nu^{CoRu}}{m_\nu^{YIG}} \right) \cdot m_\nu^{YIG} \qquad (11)$$

with m_ν^i being the normalized magnetization reversal contribution at frequency ν for layer i. If both layers would now show a synchronous magnetic reversal, $\frac{m_\nu^{CoRu}}{m_\nu^{YIG}}$ would be equal to 1, making Eq. (11) de facto identical to Eq. (10) and produce the same signal pattern and identical phase angle values $\phi_{\tilde{\beta}_\nu}$ for all frequencies ν. This is obviously not the case here for our $x = 0.95$ sample, which according to Eq. (11) means that $\frac{m_\nu^{CoRu}}{m_\nu^{YIG}}$ is neither equal to 1 nor the same value for different frequencies ν. Thus, the data in Figs. 4 (e) – (h) demonstrate that the magnetization reversal of the YIG and the CoRu insertion layers, once they are ferromagnetic cannot be synchronous, but instead must be independent from each other.

The fact that this independence holds for all our samples can be seen in Fig. 4(i), where we show the phase angle difference $\phi_{\tilde{\beta}_{3\omega}}$ - $\phi_{\tilde{\beta}_\omega}$ between the $\tilde{\beta}_\nu$ values for 3ω and ω, which are the two largest signal contributions. For $x = 0.75$, the phase difference is zero, because the CoRu is not magnetic at room temperature and thus the second term of Eq. (11) vanishes. From $x = 0.80$ onwards, a small magnetization and thus magnetic signal is existent in our insertion layers, and a phase shift occurs in our samples between the fundamental (ω) and higher harmonic (3ω, 5ω, 7ω) signal pattern. The phase shift increases with x, primarily because $\tilde{\beta}_{CoRu}$ increases with x according to Eq. (9), making the two terms in Eq. (11) more equal in size and thus, it increases the observable phase shift that originates from the different reversal behavior in YIG and CoRu. For $x = 1.00$, the phase shift reduces significantly, because the magneto-optical signal is now dominated by the Co insertion layer, as shown in Fig. 3(a), and thus the comparatively small first term in Eq. (11) can only produce a small phase shift. Overall, these data clearly demonstrate that the magnetization reversal of the YIG films and the CoRu

insertion layers are very different, so that we must conclude that they are independent and at most very weakly coupled magnetic entities in our overall sample structure.

4. Conclusions and Outlook

Our experimental study here demonstrates that with T-MOKE ellipsometry it is possible to determine the magneto-optical and magnetic properties of insertion layers, even if they are superimposed onto much bigger magnetic signals from the base or background structure. Hereby, it is especially valuable that one has full and precise quantitative access to the complex value of the T-MOKE reflection matrix component $\tilde{\beta}$, because small magneto-optical insertion layer contributions might not actually increase the absolute size of $\tilde{\beta}$, given that their contribution might be out-of-phase with the background signal. Thus, phase information for $\tilde{\beta}$, i.e. $\phi_{\tilde{\beta}}$, turns out to be crucially important in the pursuit of detecting small magnetization values reliably as we have demonstrated here. Given that there is nothing unique about the specific material system and sample geometry that we have chosen here, our T-MOKE ellipsometry approach should be universally applicable, including for the characterization of multilayers consisting of metallic films only. In addition, the detailed signal analysis allowed us to demonstrate that the CoRu insertion layers in our samples exhibit a magnetization reversal behavior that is independent from the YIG layer underneath, which is very valuable additional information, given that this clearly indicates that both magnetic entities are either not or only very weakly coupled. This furthermore explains the required total thickness of the insertion layer that is needed to generate ferromagnetism in the first place, observed to be about 1.7 nm for pure Co, which is rather thick and would seem highly anomalous, if the magnetism in the YIG and insertion layer films were actually coupled, because one would have expected the YIG film to support ferromagnetism in coupled insertion layers.

In the future, it will not only be interesting to utilize our findings and especially our T-MOKE ellipsometry for other samples, but it will be interesting to explore, if an even more elaborate analysis of the frequency dependence of the measured signals, using possibly even higher harmonics, can be utilized to analyze the magnetization

reversal in more than two magnetic layers in an independent and reliable fashion. This, however, extends far beyond the scope of the present work.

Acknowledgements

References

[1] A. Fert, Rev. Mod. Phys. **80,** 1517 (2008).

[2] F. Hellman *et al.*, Rev. Mod. Phys. **89**, 025006 (2017).

[3] P. Grünberg, R. Schreiber, Y. Pang, M. B. Brodsky, and H. Sowers, Phys. Rev. Lett. **57**, 2442 (1986).

[4] S. S. P. Parkin *et al.*, Phys. Rev. Lett. **64,** 2304 (1990).

[5] E. Y. Vedmedenko, P. Riego, J. A. Arregi, and A. Berger, Phys. Rev. Lett. **122**, 257202 (2019).

[6] E. Y. Vedmedenko et al., J. Phys. D: Appl. Phys. **53** 453001 (2020).

[7] P. F. Carcia, A. D. Meinhaldt, and A. Suna, Appl. Phys. Lett. **47**, 178 (1985).

[8] H. J. G. Draaisma, W. J. M. de Jonge, and F. J. A. den Broeder, J. Magn. Magn. Mater. **66**, 351 (1987).

[9] C.-J. Lin, G.L. Gorman, C.H. Lee, R.F.C. Farrow, E.E. Marinero, H.V. Do, H. Notarys, C.J. Chien, J. Magn. Magn. Mater. **93**, 194 (1991).

[10] M. N. Baibich, J. M. Broto, A. Fert, F. Nguyen Van Dau, F. Petroff, P. Etienne, G. Creuzet, A. Friederich, and J. Chazelas, Phys. Rev. Lett. **61**, 2472 (1988).

[11] G. Binasch, P. Grünberg, F. Saurenbach, and W. Zinn, Phys. Rev. B **39**, 4828(R) (1989).

[12] J.C Slonczewski, J. Magn. Magn. Mater. **247**, 324 (2002).

[13] D. Hou, Z. Qiu, J. Barker, K. Sato, K. Yamamoto, S. Vélez, J. M. Gomez-Perez, L. E. Hueso, F. Casanova, and E. Saitoh, Phys. Rev. Lett. **118**, 147202 (2017).

[14] F. Nakata et al., Jpn. J. Appl. Phys. **58** SBBI04 (2019)

[15] T. Niimura *et al.*, Phys. Rev. B **102,** 094411 (2020).

[16] P. Bruno and C. Chappert, Phys. Rev. B **46**, 261 (1992).

[17] J. E. Ortega, F. J. Himpsel, G. J. Mankey, and R. F. Willis, Phys. Rev. B **47**, 1540 (1993).

[18] R. K. Kawakami, E. Rotenberg, E. J. Escorcia-Aparicio, H. J. Choi, T. R. Cummins, J. G. Tobin, N. V. Smith, and Z. Q. Qiu, Phys. Rev. Lett. **80**, 1754 (1998).

[19] G. Schütz, R. Wienke, and W. Wilhelm, J. Appl. Phys. **67**, 4456 (1990).

[20] N. Nakajima, T. Koide, T. Shidara, H. Miyauchi, H. Fukutani, A. Fujimori, K. Iio, T. Katayama, M. Nývlt, and Y. Suzuki, Phys. Rev. Lett. **81**, 5229 (1998).

[21] P. Fischer and H. Ohldag, Rep. Prog. Phys. **78**, 094501 (2015).

[22] Z. Q. Qiu and S. D. Bader, Rev. Sci. Inst. **71**, 1243 (2000).

[23] A. Berger, S. Knappmann and H.P. Oepen, J. Appl. Phys. **75**, 5598 (1994).

[24] P. Vavassori, Appl. Phys. Lett. **77**, 1605 (2000).

[25] P. Riego, S. Velez, J. M. Gomez-Perez, J. A. Arregi, L. E. Hueso, F. Casanova, and A. Berger, Appl. Phys. Lett. **109**, 172402 (2016).

[26] P. Riego, S. Tomita, K. Murakami, T. Kodama, N. Hosoito, H. Yanagi, and A. Berger, J. Phys. D: Appl. Phys. **50**, 19LT01 (2017).

[27] R. Atkinson, J. Phys.: Cond. Mat. **12**, 7735 (2000).

[28] R. Atkinson et al., J. Phys.: Cond. Mat. **13**, 691 (2001).

[29] R. Weber, C. Martín Valderrama, L. Fallarino, and A. Berger, Phys. Rev. B **102**, 214434 (2020).

[30] Figen Ece Demirer et al., J. Appl. Phys. **129**, 163904 (2021).

[31] M. R. Pufall, C. Platt, and A. Berger, J. Appl. Phys. **85**, 4818 (1999).

[32] G. Pénissard, P. Meyer, J. Ferré, and D. Renard, J. Magn. Magn. Mater. **146**, 55 (1995).

[33] J. Hamrle et al., Phys. Rev. B **66,** 224423 (2002).

[34] E. Oblak *et al.*, J. Phys. D: Appl. Phys. **53,** 205001 (2020).

[35] O. Idigoras, U. Palomares, A. K. Suszka, L. Fallarino, and A. Berger, Appl. Phys. Lett. **103**, 102410 (2013).

[36] C. Martín Valderrama, M. Quintana, T. Yamauchi, Y. Hamada, Y. Kurokawa, H. Yuasa, and A. Berger, *in preparation.*

[37] E. Oblak *et al.*, J. Phys. D: Appl. Phys. **50**, 23LT01 (2017).

[38] J.M. Marín Ramírez et al., Phys. Rev. E **102**, 022804 (2020).

[39] M. Quintana et al., Phys. Rev. B **102**, 094436 (2020).

[40] G. Traeger, L. Wenzel and A. Hubert, Phys. Status Solidi **131**, 201 (1992).

[41] L. Fallarino, P. Riego, B. J. Kirby, C. W. Miller, and A. Berger, Materials **11**, 251 (2018).

Figure Captions

Figure 1:
(a) schematic of the ellipsometric T-MOKE system consisting of a Laser light source, a first polarizer P$_1$, a quarter wave plate QWP, a second polarizer P$_2$ and a Photodetector. The polarization angle θ_1 for P$_1$, the orientation angle Φ_2 for QWP and the polarization angle θ_2 for P$_2$ are given as the angular distance between each optical element's axis and the optical plane-of-incidence, utilizing the sign convention displayed here as positive rotation sense. The Sample under investigation is located inside the gap of an Electromagnet that produces a magnetic field transverse to the plane-of-incidence. The path of the laser light is indicated in the figure; (b) schematic of the multilayer structure of our samples containing a 2 nm thick Co$_x$Ru$_{1-x}$ alloy insertion layer with Co concentration x in the range of $0.75 - 1.00$.

Figure 2:
(a)-(g) experimental T-MOKE ellipsometry maps, displaying the magnetic field induced relative intensity change $\Delta I/I$ at saturation as a function of the orientation of the optical elements P$_2$ and QWP, given by their distance from the extinction point, i.e. $\tilde{\theta}_2$ and $\tilde{\Phi}_2$, respectively; (h)-(n) show the corresponding least-squares fits, according to Eq. (4) with the respective R^2-values being displayed inside each sub-figure. On top of each column, the specific sample is identified by its Co$_x$Ru$_{1-x}$ alloy concentration x (or by the label YIG for the reference sample without insertion layer). On the right side, the color scale associated with the displayed $\Delta I/I$ values is defined.

Figure 3:
Measured Co concentration x dependence of (a) abs($\tilde{\beta}$), (b) $\phi_{\tilde{\beta}}$, and (c) the extracted insertion layer magnetization M, normalized to the pure Co film magnetization M_{Co}, according to Eq. (9). The solid green lines in (a) and (b) are the predicted values for abs($\tilde{\beta}$), and $\phi_{\tilde{\beta}}$ according to Eq. (9), shown in comparison to the experimental data, which are shown as symbols; for $x = 1.00$ there are two data points displayed, measured on two separately fabricated samples that are nominally identical; (a) also displays the abs($\tilde{\beta}$) value for the YIG reference sample without insertion layer as a dashed line; in (c) the dashed line connecting the extracted M values is a guide to the eye.

Figure 4:
Frequency separated experimental T-MOKE ellipsometry maps, measured for the reference YIG sample without insertion layer, representing (a) ω, (b) 3ω, (c) 5ω, and (d) 7ω with ω being the frequency of the applied sinusoidal magnetic field; (e)-(h) display the same type of data, measured for the sample with a Co$_{0.95}$Ru$_{0.05}$ insertion layer, representing (e) ω, (f) 3ω, (g) 5ω, and (h) 7ω; on the right side of each line, the color scale associated with the measurement values of the normalized intensity change is defined, given that the signal size changes substantially with frequency; (i) Co concentration x dependence of the measured phase shift $\phi_{\tilde{\beta}_{3\omega}}$ - $\phi_{\tilde{\beta}_\omega}$ between the $\tilde{\beta}$ phase angle determined for the higher harmonic magneto-optical response at 3ω and the one measured for the fundamental frequency ω.
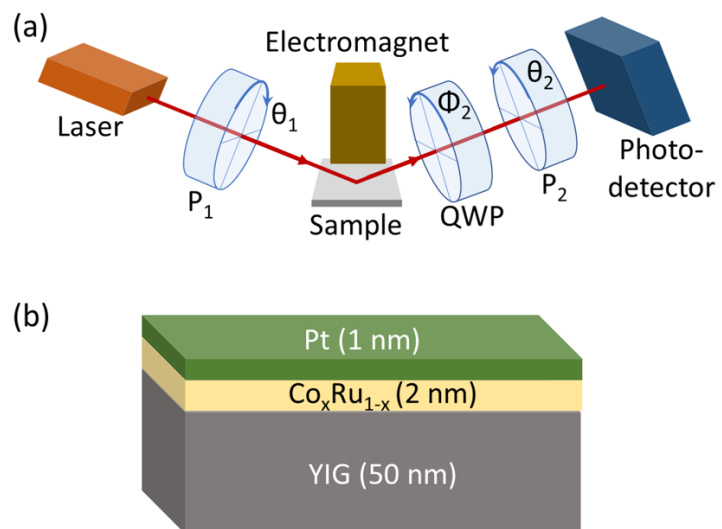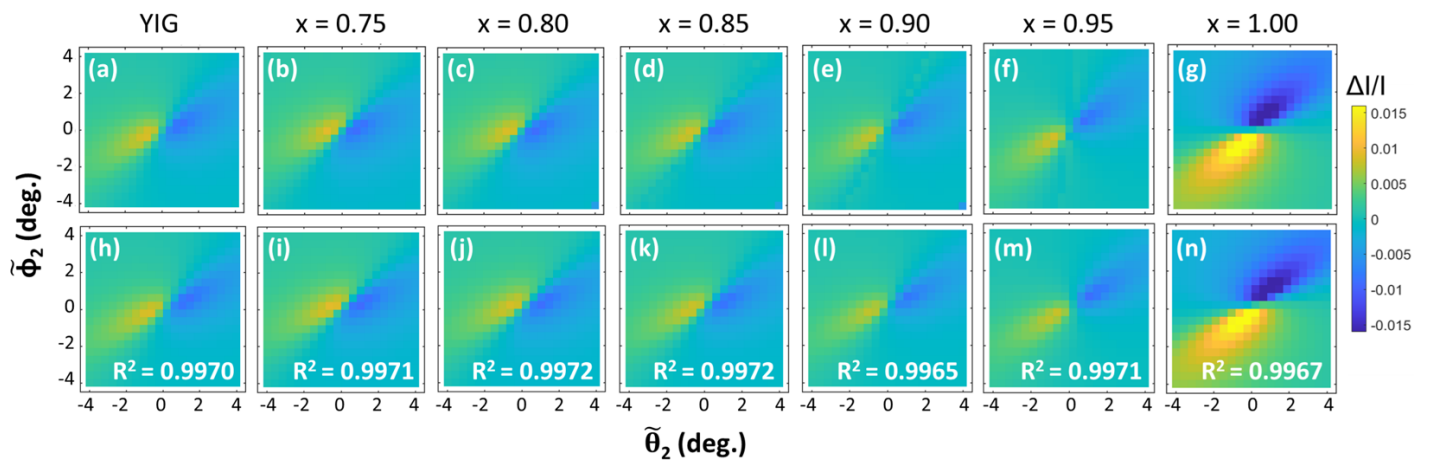
Fig. 1

(a)

(b)
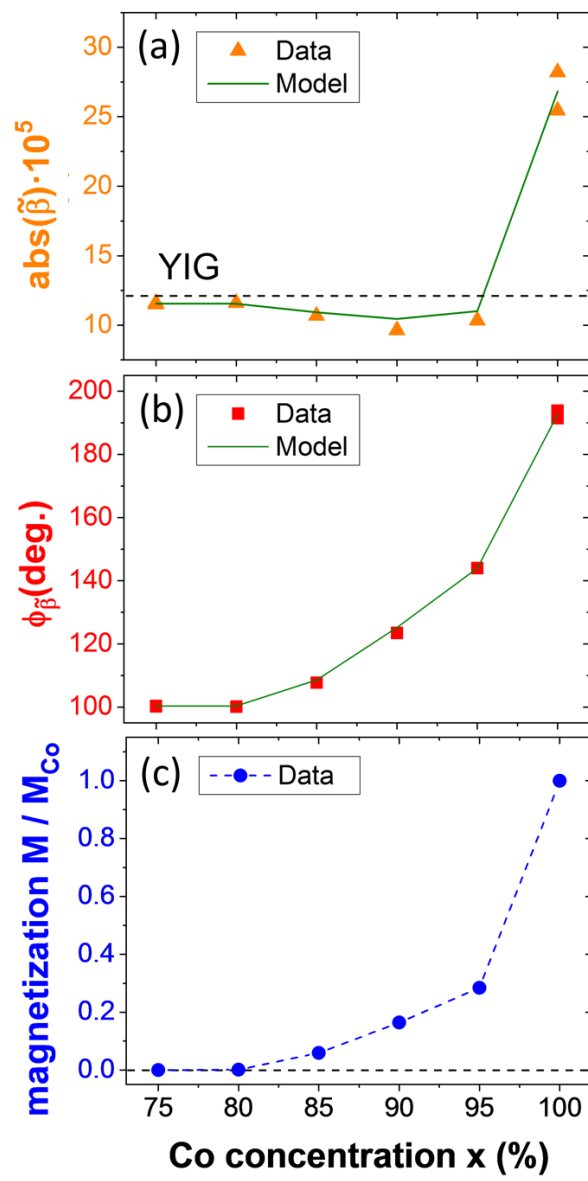
Fig. 2

Fig. 3

Fig. 4